Applied Catalysis A, General 648 (2022) 118924

Contents lists available at ScienceDirect

Applied Catalysis A, General

journal homepage: www.elsevier.com/locate/apcata

Studying the effects of processing parameters in the aerosol-assisted chemical vapour deposition of TiO_2 coatings on glass for applications in photocatalytic NO_x remediation

Yanda Wong [a], Yuankai Li [a], Zhipeng Lin [a], Andreas Kafizas [a,b,*]

[a] Department of Chemistry, Molecular Science Research Hub, Imperial College London, White City, London W12 0BZ, UK
[b] London Centre for Nanotechnology, Imperial College London, SW7 2AZ, UK

ARTICLE INFO

Keywords:
NO_x remediation
Titanium dioxide (TiO_2)
Photocatalysis
Chemical vapour deposition (CVD)
Thin films

ABSTRACT

Herein, we employ an aerosol-assisted method (AA-CVD) to produce TiO_2 on window glass and study how the process parameters affect their photocatalytic activity towards NO_x ($NO + NO_2$) remediation. A range of process parameters are explored to produce 50 unique TiO_2 coatings with wide ranging physicochemical properties. The physicochemical properties were examined using X-ray diffraction (XRD), atomic force microscopy (AFM), UV–visible transmission spectroscopy and transient absorption spectroscopy (TAS), and the photocatalytic activity towards NO gas was measured using protocol akin to the ISO (22197-1:2016). The most active sample showed an NO removal of ~14.4 ± 1.7 % and NO_x removal of ~5.4 ± 0.77 %, which was ~40 and ~25 times higher than that of a commercially available self-cleaning window. The links between the process parameters, physicochemical properties and photocatalytic activity were studied in depth, where it was seen that the three most influential physicochemical properties on the observed activity were surface roughness, charge carrier population and charge carrier lifetime. Therefore, we recommend that these properties be targeted in the rational design of more active coatings for applications in photocatalytic NO_x remediation.

1. Introduction

Nitric oxide (NO) and nitrogen dioxide (NO_2) gases are formed when fossil fuels are burnt, and are collectively known as NO_x ($NO + NO_2$) [1]. NO_x pollution causes a range of health and environmental problems. It is responsible for ground level ozone and urban smog [2]. Short-term exposure to high levels of NO_x can exacerbate asthma, inhibit lung function and even cause mortality [3]. Long-term exposure to high levels of NO_x has negative impacts on all organs, mental health and reduces life expectancy [4,5]. Most NO_x emissions are anthropogenic [6], with road transport being the greatest contributor [7].

Of the various mitigation options being explored, photocatalysts are an attractive option [8]. Photocatalysts can be applied to the surface of building materials, and using ambient light, can remedy surrounding NO_x pollution [9]. Photocatalysts are increasingly being applied in building materials to remedy air pollution [10]. Most products on the market use the photocatalyst titanium dioxide (TiO_2), which remedies NO_x through an oxidation pathway [11]. When TiO_2 absorbs light (hv) of energy greater than or equal to its bandgap energy (E_{bg}), electrons (e^-) are excited from the valence band to the conduction band; leaving behind positive holes (h^+) in the valence band [12]. The electrons can react with oxygen (O_2) in the air to form superoxide radicals (O_2^-), and the positive holes can react with ambient water (H_2O) to form hydroxyl radicals ($OH^\bullet$) [10]. These radicals oxidise NO_x, with O_2^- reacting with NO to form nitric acid (HNO_3) and $OH^\bullet$ reacting with NO_x in a sequential manner, taking NO to nitrous acid (HONO), then to NO_2, and finally to HNO_3 [13]. These reaction processes are summarised below:

$$TiO_2 \xrightarrow{hv \geq E_{bg}} e^- + h^+ \quad (1a)$$

$$e^- + O_2 \rightarrow O_2^- \quad (b)$$

$$h^+ + H_2O \rightarrow \quad \dot{O}H + H^+ \quad (1c)$$

$$O_2^- + NO + H^+ \rightarrow HNO_3 \quad (1d)$$

$$\dot{O}H + NO \rightarrow HONO \quad (1e)$$

* Corresponding author at: Department of Chemistry, Molecular Science Research Hub, Imperial College London, White City, London W12 0BZ, UK.
E-mail address: a.kafizas@imperial.ac.uk (A. Kafizas).

https://doi.org/10.1016/j.apcata.2022.118924
Received 26 August 2022; Received in revised form 30 September 2022; Accepted 22 October 2022
Available online 28 October 2022

$$\dot{O}H + HONO \rightarrow NO_2 + H_2O \quad (1\ f)$$

$$\dot{O}H + NO_2 \rightarrow HNO_3 \quad (1\ g)$$

To date, the most common building materials upon which TiO_2 has been incorporated and examined for photocatalytic NO_x remediation are concretes, paints and asphalts [10]. When such building materials have been tested using the specified ISO testing protocol (ISO 22197-1:2016 [14]) the reported photocatalytic NO removal activities range from ~7–45 % in concrete, ~14–70 % in paints, and ~14–67 % in asphalts [15]. However, studies using window glass have shown much lower photocatalytic activity towards NO removal [16], where, to our knowledge, no modified window glass product has been marketed as being capable of effectively remediating NO_x. As there is an increasing trend in cities, where air pollution is rife, to construct buildings where a high proportion of the exterior is window glass, the primary goal of this work is to develop coatings of TiO_2 on window glass that are active for photocatalytic NO_x remediation and therefore improving air quality.

Thin coatings of TiO_2 are routinely applied on window glass to provide a nominal self-cleaning function, with the first such product, Pilkington Activ™, marketed by Pilkington NSG [17]. It should be noted that Pilkington Activ™ was not designed to tackle NO_x pollution, and is not marketed for that purpose; rather, it was designed to help keep window glass cleaner and clearer. The TiO_2 coating in Pilkington Activ™ is produced using chemical vapour deposition (CVD) during the float glass production process, as the glass melt cools [18]. During the CVD process, precursors are transported over a heated substrate, where they decompose to form the desired solid coating [19]. A specific branch of CVD, aerosol-assisted CVD (AA-CVD), can provide greater flexibility in the choice of precursor, as it removes the requirement for the precursor to be volatile; replacing this with the simpler requirement that the precursor can be dissolved in a solvent that can be aerosolised [20]. This increased flexibility also means that additives, such as templating agents (i.e. surfactants) can also be incorporated and studied [21]. By changing the process parameters (e.g. precursor, deposition temperature, etc.) one can alter the physical properties of the coating formed (e.g. crystal structure, crystal size, topography, coating thickness, etc.) [22].

Herein, we employ AA-CVD to produce TiO_2 coatings on window glass and examine their photocatalytic activity towards NO gas. A range of process parameters are explored, which include the precursor (TTIP and $Ti(OBu)_4$), deposition temperature (400, 450, 500 and 550 °C), co-oxidant (IPA, EtOH and MeOH), surfactant (CTAB or SDS) and solvent used (IPA, EtOH, MeOH and toluene), to produce 50 unique TiO_2 coatings with wide ranging of physicochemical properties. Various physicochemical properties were investigated: X-ray diffraction (XRD) was used to determine the crystal phases present, unit cell volumes, average crystal size and preference for crystal growth in a particular orientation; atomic force microscopy (AFM) was used to determine the surface roughness (Rq) and roughness factor (Rf); UV–visible transmission spectroscopy was used to determine the optical bandgap energy (E_{bg}), average visible light transmittance (VLT) and film thickness; and transient absorption spectroscopy (TAS) was used to determine the population of charge carriers and their lifetime.

The links between the process parameters, physicochemical properties and photocatalytic activity towards NO gas were studied, which allowed us to generate an understanding of how the process parameters influenced the photocatalytic activity and physicochemical properties of the coating. Also, our studies of how the physicochemical properties influenced photocatalytic activity culminated in the production of a simple linear combination model, which allowed us to estimate the influence of each physicochemical property on the observed activity.

2. Experimental

2.1. Chemicals and substrates

Titanium (IV) isopropoxide (TTIP) (99 %), titanium (IV) n-butoxide ($Ti(OBu)_4$) (99 %), acetone (99 %), toluene (99.9 %), methanol (99.9 %), ethanol (99.9 %), isopropanol (99.9 %), cetrimonium bromide (CTAB) (98 %), and sodium dodecyl sulfate (SDS) (99 %) were purchased from Sigma-Aldrich and used as received. Nitrogen gas (99.99 %) was provided by BOC. Float glass substrates (50 × 100 × 2.2 mm) that contain an ultra-thin (~50 nm) SiO_2 barrier layer were provided by Pilkington NSG. The glass substrates were washed with distilled water: soap (1:1), distilled water, acetone, and isopropanol respectively, and dried in air prior to use.

2.2. Synthesis

Herein, using aerosol-assisted chemical vapour deposition (AA-CVD), the processing parameters were systematically varied to produce 50 unique TiO_2 coatings. A general scheme of the CVD process is detailed in Fig. S1. The syntheses studied herein can be segregated into 3 types, where we study (i) the effect of a co-oxidant, (ii) the effect of a surfactant and (iii) the effect of the precursor solvent on the physical properties and photocatalytic NO_x activity of the TiO_2 coatings produced.

2.2.1. The effect of co-oxidant

The layout of the CVD apparatus for this set of experiments is shown in Fig. S2a. In each experiment, TTIP (1.00 mL, 3.38 mmol) was dissolved in 25 mL of toluene. An aerosol mist of the precursor solution was generated (Johnson-Matthey Liquifog piezoelectric device). Concurrently, the vapours of a co-oxidant (Ox), generated by heating (Electrothermal EMA0100/CEB Electromantle) 50 mL of an oxygen source (isopropanol = IPA, ethanol = EtOH, methanol = MeOH or none = NONE). The mist (2 $L.min^{-1}$) and vapours (2 $L.min^{-1}$) were carried using an inert nitrogen gas carrier, combined, and then carried into the reactor where the float glass substrate was located at a total flow rate of 4 $L.min^{-1}$. Depositions were carried out at 400, 450, 500 and 550 °C for 15 min. Post deposition, the reactor chamber was allowed to cool naturally to room temperature before the sample was removed.

Samples from these reactions had a naming scheme of "precursor, effect studied, co-oxidant used, deposition temperature". For example, a sample made at 400 °C using IPA as a co-oxidant is labelled TTIP-Ox-IPA-400. A full list of the sample names and reaction conditions are provided in Table S1.

2.2.2. The effect of surfactant

The layout of the CVD apparatus for this set of experiments is shown in Fig. S2b. In each experiment, either TTIP (1.00 mL, 3.38 mmol) was dissolved in 25 mL of ethanol or $Ti(OBu)_4$ (1.00 mL, 2.94 mmol) was dissolved in 25 mL of methanol. Inside these precursor solutions, the surfactant (Surf) CTAB (0, 0.25, 0.50, 0.75 or 1.0 g) or SDS (0, 0.025, 0.050, 0.075, 0.10, 0.25, 0.50, 0.75 or 1.0 g) was added. An aerosol mist was generated and carried to the reactor using nitrogen with a flow rate of 2 $L.min^{-1}$. For reactions using TTIP, depositions were carried out at 450 °C, and for reactions using $Ti(OBu)_4$, depositions were carried out at 550 °C. All reactions were carried out for 15 min. Post deposition, the reactor chamber was allowed to cool naturally to room temperature before the sample was removed.

Samples from these reactions had a naming scheme of "precursor, effect studied, surfactant used, mass of surfactant". For example, a sample made using TTIP and 0.25 g of CTAB is labelled TTIP-Surf-CTAB-0.25 g. A full list of the sample names and reaction conditions are provided in Table S1.

2.2.3. The effect of solvent

The layout of the CVD apparatus for this set of experiments is shown in Fig. S2b. In each experiment, $Ti(OBu)_4$ (1.00 mL, 2.94 mmol) was dissolved in 25 mL of solvent (Sol) (methanol = MeOH, ethanol = EtOH, toluene = Toluene and isopropanol = IPA). An aerosol mist was generated and carried to the reactor by nitrogen gas with a flow rate of 2 $L.min^{-1}$. Depositions were carried out at 400, 450, 500 and 550 °C for 15 min. Post deposition, the reactor chamber was allowed to cool naturally to room temperature before the sample was removed.

Samples from these reactions had a naming scheme of "precursor, effect studied, precursor solvent used, deposition temperature". For example, a sample made at 400 °C using MeOH as a precursor solvent is labelled $Ti(OBu)_4$-Sol-MeOH-400. A full list of the sample names and reaction conditions are provided in Table S1.

2.3. Physical characterisation

2.3.1. XRD

X-ray diffraction (XRD) patterns of the centre of each coating were measured with a Bruker D2 Phaser diffractometer with parallel beam optics equipped with a Lynx-Eye detector. X-rays were generated using a Cu source (V = 30 kV, I = 10 mA) with Cu $K_{\alpha1}$ ($\lambda = 1.54056$ Å) and Cu $K_{\alpha2}$ radiation ($\lambda = 1.54439$ Å) emitted with an intensity ratio of 2:1. Patterns were collected between $10° \leq 2\theta \leq 70°$ with a step size of 0.04° for a collection time of 1 s per step. Patterns were compared to standards from the Physical Sciences Data-Science (PSDS) database [23]. Lattice parameters and the average crystallite size of each sample was determined from a Le Bail model, which was fit to each diffraction pattern using GSAS-EXPGUI software [24]. Where both anatase and rutile phases were observed, the anatase phase fraction was determined from a refined scale factor, which was estimated by summing the total counts for each phase (Equation 2), where S is the refined scale factor, ρ is the density obtained from the modelling, V is the unit cell volume obtained from the modelling, and subscripts A and R represent anatase and rutile, respectively [25].

$$\text{Anatase(wt.}\quad\%) = \left(\frac{S_A\rho_A{V_A}^2}{S_A\rho_A{V_A}^2 + S_R\rho_R{V_R}^2}\right) \times 100 \tag{2}$$

The average crystallite size was also determined using the Scherrer relationship (Eq. 3) [26], where ρ is the average crystallite size in Å, K is the Scherrer constant and set at 0.9, and LX is the Lorentzian isotropic crystallite size broadening coefficient obtained from the model [27].

$$\rho \quad (\text{nm}) = \quad 180,000\text{K}/(\pi \quad \bullet \text{LX}) \tag{3}$$

The degree of preferred orientation in the (101), (200) and (211) crystal planes in anatase were also quantified by calculating the texture coefficient $P(hkl)_i$ using the Harris method [28], where $I(hkl)_i$ is the measured peak intensity for the hkl plane, $I_0(hkl)_i$ is the standard intensity of the hkl plane [29–31], and n is the number of diffraction peaks considered (Eq. 4).

$$P(hkl)_i = I(hkl)_i \Big/ I_0(hkl)_i \Big/ \left(\frac{1}{n}\right)\sum\nolimits_i^n \left(I(hkl)_i / I_i(hkl)_i\right) \tag{4}$$

2.3.2. SEM and AFM

Scanning electron microscopy (HR-SEM) was performed on the centre all coatings to image the surface morphology using a Zeiss Auriga 60 SEM at an accelerating voltage of 5 keV. A Q150T S sputter coater with a 0.3 mm thick chromium target was used prior to SEM to coat samples with an ultra-thin conductive chromium layer to reduce charging. ImageJ was used to process images.

Atomic Force Microscopy (AFM) was performed on the centre of all coatings using an Agilent 5500 in tapping mode using aluminium-coated silicon tips (Tap300AL-G). A scan resolution of 256 lines per sample with an area size of 5 × 5 μm was used. The majority of samples were imaged (33 of the 50 samples produced herein). Images were processed and analysed using Gwyddion 2.60, from which the root mean square roughness (Rq) [32] and roughness factor (Rf) [33] were derived.

2.3.3. UV–visible absorption spectroscopy

UV–visible absorption spectroscopy was carried out on the centre of all samples using a Shimadzu UV-2600 Spectrometer over a wavelength range of 200–1000 nm. The indirect allowed bandgap (E_{bg}) energy of each sample was determined from a Tauc plot [34] Their average visible light transmittance (VLT) of each sample was determined by averaging transmission data from 380 to 750 nm [35] Where samples showed interference fringes, film thickness was also determined using the Swanepoel method [36] using a refractive index value of TiO_2 from the literature [37].

2.4. Photocatalytic NOx activity

The photocatalytic NO_x activity of all TiO_2 samples produced herein, and a Pilkington Activ™ commercial standard, was examined in line with ISO protocol (ISO 22197-1:2016 [14]), with some minor modifications. In the ISO test, the activity of a ~5.0 x ~10.0 cm sized sample is examined in a plug flow reactor of specified dimensions (5.0 ± 0.5 mm headspace). NO gas (1.0 ± 0.05 ppm) in humid air (50 ± 3 % relative humidity) is passed over the sample at a rate of 3.0 ± 0.15 $L.min^{-1}$ (Bronkhorst, el-flow select). In the ISO test, a sample is exposed to the gas for 30 mins in the dark, then 300 mins under UVA irradiation (2 × 15 W black bulbs; λ_{max} = 352 nm; 1.0 ± 0.05 $mW.cm^{-2}$) and then 30 mins in the dark. Given the large number of samples studied herein (50 samples), some deviations from the ISO test were made to reduce the analysis time. Herein, the sample was exposed to the gas for 15 mins in the dark, then 60 mins under UVA irradiation, and then 15 mins in the dark. Changes in NO_x levels were measured every minute (the average of 4 ×15 s measurement cycles) using a chemiluminescence analyser (Ecotech Serinus® 40). A typical reaction profile is shown in Fig. S3.

For every test, the average NO removal (%), average NO_x removal (%), HNO_3 selectivity (%) and NO deposition velocity (v_d, mm/s) were determined using the equations below:

$$\text{NO removal}(\%) = \frac{[\text{NO}]_{in} - [\text{NO}]_{out}}{[\text{NO}]_{in}} \times 100\% \tag{5a}$$

$$\text{NO}_x\text{removal}(\%) = \frac{[\text{NO}_x]_{in} - [\text{NO}_x]_{out}}{[\text{NO}_x]_{in}} \times 100\% \tag{5b}$$

$$\text{HNO}_3\text{selectivity}(\%) = 100\% - \left(\frac{[\text{NO}_2]_{out}}{[\text{NO}]_{in} - [\text{NO}]_{out}} \times 100\%\right) \tag{5c}$$

$$v_d \quad (\text{mm/s}) = \log_e([\text{NO}]_{in}/[\text{NO}]_{out}) \times \text{F/A} \tag{5d}$$

where $[NO]_{in}$ and $[NO_x]_{in}$ are the average NO and NO_x levels seen over the two 15 min dark periods, respectively, and $[NO]_{out}$, $[NO_x]_{out}$ and $[NO_2]_{out}$ are the average NO, NO_x and NO_2 levels seen over the 60 min UVA exposure period, respectively, F is the flow rate of gas (mm^3/s) and A is the area of sample examined (mm^2). It should be understood that one limitation of using chemiluminescence to determine NO_x speciation is that it cannot distinguish between HONO and NO_2 [38]. Therefore, in the determination of HNO_3 selectivity, the assumption is made that only NO_2 and HNO_3 products are formed during the photocatalytic oxidation of NO gas.

2.5. Transient absorption spectroscopy

The transient absorption decay kinetics of the centre of all samples was measured from the microsecond to second timescale in transmission mode. A Nd:YAG laser (OPOTEK Opolette 355 II, ~6 ns pulse width) was used as the excitation source, generating 355 nm UV light from the third

harmonic (~2.54 mJ.cm^{-2} per pulse, repetition rate of 0.67 Hz). The probe light was a 100 W Bentham IL1 quartz halogen lamp. A long pass filters (Comar Instruments, $\lambda > 420$ nm) was placed between the lamp and sample to prevent excitation of the sample by the probe light. Transient changes in transmission through the sample was collected by a 2" diameter, 2" focal length lens and relayed to a monochromator (Oriel Cornerstone 130) and measured at a fixed wavelength of 650 nm. Time-resolved changes in transmission were collected using a Si photodiode (Hamamatsu S3071). Data at times faster than 3.6 ms was recorded by an oscilloscope (Tektronics DPO3012) after passing through an amplifier box (Costronics), whereas data slower than 3.6 ms was recorded on a National Instrument DAQ card (NI USB-6251). Each kinetic trace was obtained from the average of 200 laser pulses. Acquisitions were triggered by a photodiode (Thorlabs DET10A) from laser scatter. Data was acquired and processed using home-built software written in Labview. All measurements were carried out in air.

2.6. Linear combination modelling

Linear combination modelling, described in more detail in Section 3.5.2.5, was carried out in Excel using the Solver tool and the Evolutionary Solver Method.

3. Results and discussion

Given the large number of samples produced and investigated herein, we have split their detailed physicochemical and functional characterisation into 3 parts, by the synthetic effect studied. The effect of introducing a co-oxidant during coating growth (16 samples) is presented in the main text (Section 3.1). And to avoid undue repetition, the effects of adding a surfactant to the precursor flask (18 samples) and solvent used to dissolve the precursor (16 samples) are presented and discussed in the Supporting Information (Sections SI3.2 and SI3.3, respectively). In Section 4, we discuss the results from this study as a collective.

3.1. The effect of co-oxidant

3.1.1. Appearance and XRD

Most of the coatings produced in this series appeared smooth and transparent (Fig. 1a and Fig. S4), with the exception of those produced using MeOH as a co-oxidant at 500 and 550 °C, which appeared rougher and more hazy. Most films displayed a series of interference colour bands, primarily oscillating between red, yellow, green and purple caused by changes in film thickness across the coating [39]. The

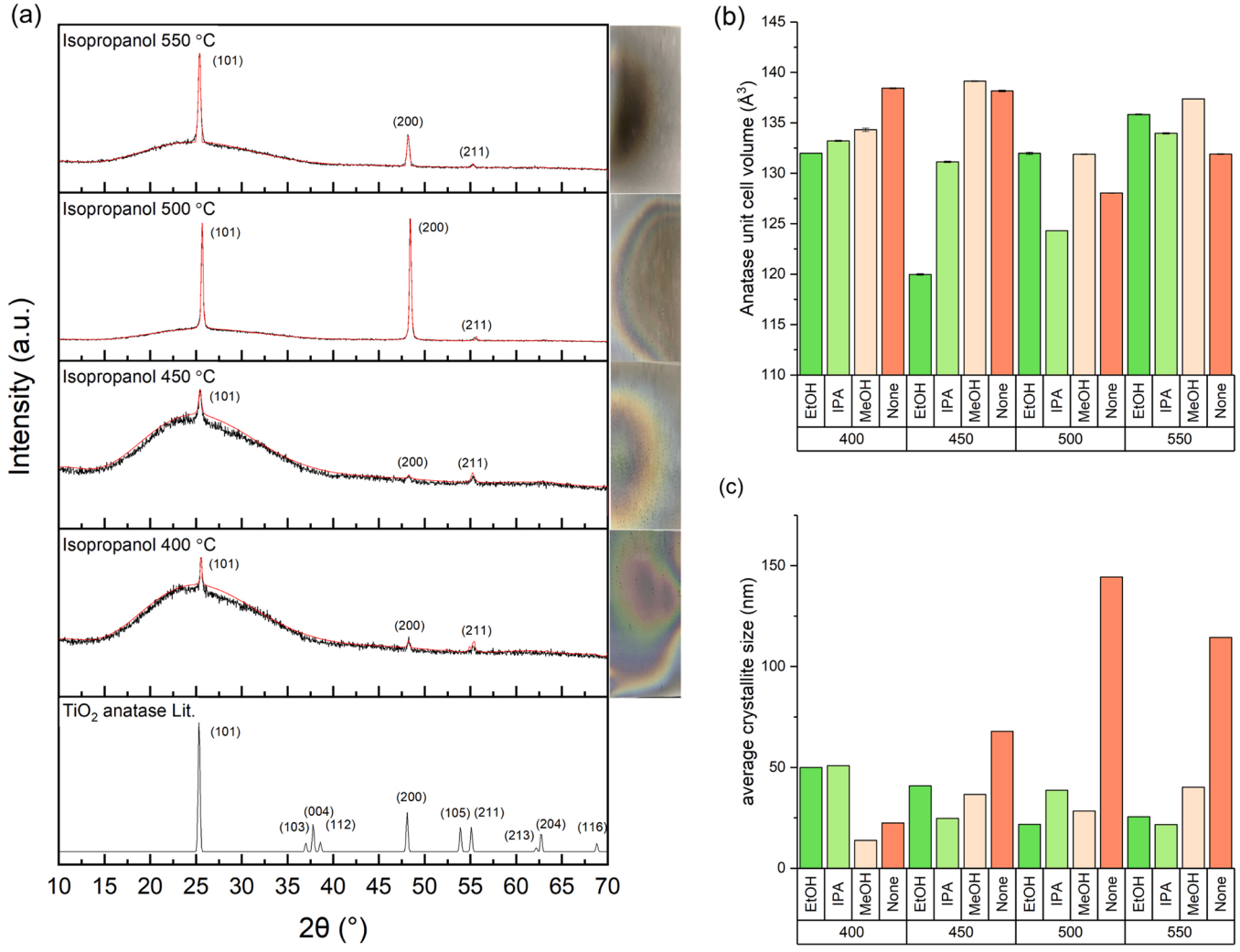

Fig. 1. (a) XRD patterns (black) and their fit models (red) plot alongside digital images of the TiO_2 coatings for the series where the effect of an IPA co-oxidant was studied, with depositions carried out at 400, 450, 500 and 550 °C. Bar chart plots of the (b) anatase unit cell volume (Å [3]) and (c) average crystallite size (nm) for all TiO_2 coatings in the co-oxidant series, grouped by deposition temperature (400, 450, 500 and 550 °C) and then by co-oxidant used (IPA = isopropanol; EtOH = ethanol; MeOH = methanol; None = no co-oxidant used). (For interpretation of the references to colour in this figure legend, the reader is referred to the web version of this article.)

contours of the colour bands indicated that most coatings were thickest at the centre, which was attributed to the higher temperature experienced at the centre of the reactor; owing to the cold-wall reactor design [40]. All coatings passed the Scotch™ tape test [41], but could be scratched by a diamond tipped pen. The coatings in this series also showed varying degrees of coverage of the glass substrate and a brown tinge; most likely due to carbon contamination [42]. Those produced without a co-oxidant showed the most inconsistent coverage, and those produced using EtOH and IPA at 550 °C showed the strongest brown tinge.

XRD indicated that all coatings in this series contained anatase TiO_2 alone ($I4_1/amd$, $a = b = 3.7710(9)$ Å, $c = 9.430(2)$ Å [43]), with the exception of sample TTIP-Ox-MeOH-550, which also contained ~1/3 rutile TiO_2 ($P4_2/mnm$, $a = b = 4.6257(1)$ Å, $c = 2.9806(1)$ Å [44]) (Table S2). With regards to the anatase unit cell volume, there was no discernible trends between the use of co-oxidant or deposition temperature (Fig. 1b); however, it should be noted that samples in this series tended to show a contracted unit cell with respect to a standard (~134.1 Å [3]), with samples TTIP-Ox-EtOH-450 and TTIP-Ox-IPA-500 showing highly contracted unit cells. With regards to the average crystal size, the use of EtOH, IPA and MeOH co-oxidants resulted in lower average crystal size compared with the use of no co-oxidant (Fig. 1c). The smaller average crystallite size suggests that alcohols hinder crystal growth, which may be attributed to the dehydration of alcohols on TiO_2 surfaces that may inhibit agglomeration [45]. No discernible relationships were found between the average anatase crystallite size and deposition temperature. Texturing coefficients for the preferred crystal growth in the anatase (101), (200), and (211) planes were determined (Fig. S5). No discernible relationships were seen between the co-oxidant used or deposition temperature, with the exception that there is a decreased tendency to grow on the anatase (200) and (211) planes when the co-oxidant MeOH is used [28].

3.1.2. SEM and AFM

Top down SEM images of all samples produced in the co-oxidant series are presented, grouped by the co-oxidant used, for EtOH (Fig. 2), IPA (Fig. S6), MeOH (Fig. S7) and no co-oxidant (Fig. S8). It was found that the average particle size for samples made with IPA and no co-oxidant tended to decrease with increasing deposition temperature, whereas those made with the co-oxidants EtOH and MeOH showed the opposite trend. Average particle size was lowest for the coating grown at 450 °C using the co-oxidant EtOH (~50 nm; sample TTIP-Ox-EtOH-450). The coating made using the co-oxidant IPA at 550 °C were needle-like, similar to those produced by Zhang et al. [46]. Similarly, a rice-like morphology was seen in the coating made at 400 °C with the co-oxidant MeOH and became rounded crystallites at 450 °C. While the sample at 500 °C showed random particle shapes and sizes, well-defined angular crystallites were observed at 550 °C, similar to those observed by Edusi et al. [47]. At 400 °C, the sample with no co-oxidant showed rice-like morphology, and at 450 °C, needles were formed, similar to those observed by Taylor et al. [48]. At higher temperatures, the crystallites became more rounded, with clear nucleation centres present in coatings made at 500 °C.

AFM images of select samples from the co-oxidant series were measured. An example 3D image for sample TTIP-Ox-IPA-500 is shown in Fig. S9a, and a plot of the surface roughness of all samples measured in this series is shown in Fig. S9b. All surface roughness values are collated in Table 1. The limited number of samples studied meant that the effect of the synthesis parameters could not be fully explored. However, what can be said for samples grown at 500 °C, is that the use of a co-oxidant source increased surface roughness compared with the case when no co-oxidant was used. At 550 °C, the trend was less clear, however the sample produced using the co-oxidant MeOH show significantly higher surface roughness than all other samples measured in this series.

3.1.3. UV–visible absorption spectroscopy

UV–visible transmission spectroscopy was conducted on all samples in the co-oxidant series. Example UV–visible transmission patterns are shown for the series of TiO_2 coatings grown using no co-oxidant in Fig. S10a. All samples showed similar behaviour, displaying a band edge at ~350 nm that increased to high levels of transmission in the visible. What was notably different between samples was the number of oscillations observed - caused by the alternation between constructive and destructive interferences of light travelling through each sample. This phenomenon, dubbed the Swanepoel effect, is seen in coatings of high

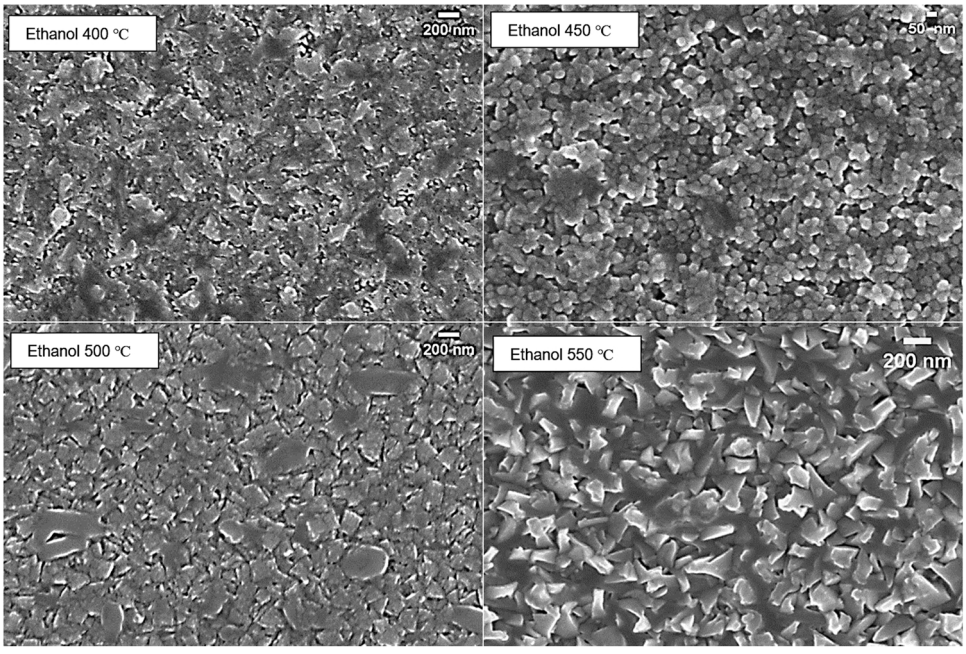

Fig. 2. Top-down SEM images for the series of TiO_2 coatings where the effect of an ethanol co-oxidant was studied, with depositions carried out at 400, 450, 500 and 550 °C.

Table 1
Summary of the physical and photocatalytic functional properties (and their associated errors) for all TiO_2 coatings in the oxidant series.

Sample name	AFM		UV–vis			Photocatalytic NO_x activity			
	Rq (nm)	Rf	E_{bg} (eV)	VLT (%)	l (nm)	NO red (%)	NO_x red (%)	HNO_3 select (%)	NO v_d (mm/s)
TTIP-Ox-IPA-400	*nm*	*nm*	3.40 ± 0.06	68.1 ± 0.7	169 ± 6	0.09 ± 0.15	0.21 ± 0.15	*un*	0.01 ± 0.01
TTIP-Ox-IPA-450	*nm*	*nm*	3.18 ± 0.06	58.3 ± 0.5	172 ± 7	2.09 ± 0.49	0.72 ± 0.25	35 ± 20	0.21 ± 0.02
TTIP-Ox-IPA-500	72.4	1.12	3.23 ± 0.04	68.0 ± 0.6	605 ± 3	6.80 ± 1.69	0.20 ± 0.19	3 ± 33	0.68 ± 0.07
TTIP-Ox-IPA-550	11.7	1.19	3.42 ± 0.04	75.3 ± 0.5	295 ± 20	2.42 ± 0.55	0.70 ± 0.22	29 ± 24	0.24 ± 0.02
TTIP-Ox-EtOH-400	*nm*	*nm*	3.29 ± 0.07	67.5 ± 0.5	236 ± 3	2.77 ± 0.47	1.02 ± 0.23	37 ± 17	0.26 ± 0.02
TTIP-Ox-EtOH-450	*nm*	*nm*	3.40 ± 0.01	71.7 ± 0.4	253 ± 16	0.71 ± 0.19	0.14 ± 0.14	20 ± 26	0.06 ± 0.01
TTIP-Ox-EtOH-500	21.7	1.11	3.29 ± 0.03	68.0 ± 0.5	512 ± 4	1.53 ± 0.36	0.52 ± 0.17	34 ± 21	0.14 ± 0.02
TTIP-Ox-EtOH-550	20.8	1.16	3.33 ± 0.06	60.4 ± 0.5	364 ± 4	2.57 ± 0.57	0.16 ± 0.37	6 ± 28	0.22 ± 0.02
TTIP-Ox-MeOH-400	*nm*	*nm*	3.44 ± 0.03	72.4 ± 0.5	302 ± 9	2.50 ± 0.54	0.87 ± 0.29	35 ± 18	0.23 ± 0.02
TTIP-Ox-MeOH-450	*nm*	*nm*	3.32 ± 0.05	68.8 ± 0.5	600 ± 21	2.66 ± 0.47	1.07 ± 0.23	40 ± 18	0.25 ± 0.02
TTIP-Ox-MeOH-500	17.9	1.10	3.35 ± 0.03	70.7 ± 0.4	187 ± 6	0.66 ± 0.22	0.15 ± 0.09	23 ± 42	0.06 ± 0.01
TTIP-Ox-MeOH-550	144	1.35	2.92 ± 0.04	48.5 ± 1.7	*np*	6.65 ± 1.03	1.48 ± 0.23	22 ± 17	0.64 ± 0.05
TTIP-Ox-None-400	*nm*	*nm*	3.21 ± 0.04	70.2 ± 0.4	392 ± 13	0.57 ± 0.14	0.18 ± 0.12	32 ± 28	0.05 ± 0.01
TTIP-Ox-None-450	*nm*	*nm*	3.37 ± 0.02	61.8 ± 0.4	1058 ± 14	2.65 ± 0.64	0.54 ± 0.29	20 ± 25	0.24 ± 0.03
TTIP-Ox-None-500	11.3	1.08	3.20 ± 0.08	70.4 ± 0.2	368 ± 11	6.35 ± 0.80	1.26 ± 0.25	20 ± 14	0.64 ± 0.03
TTIP-Ox-None-550	17.2	1.06	3.23 ± 0.08	73.4 ± 0.4	592 ± 4	0.50 ± 0.23	0.19 ± 0.11	39 ± 40	0.05 ± 0.01

Rq = root mean squared roughness; Rf = roughness factor; Ebg = indirect optical bandgap; VLT = average visible light transmittance (380 to 750 nm); l = film thickness; NO red (%) = NO reduction; NOx red (%) = NOx reduction (%); HNO3 select (%) = selectivity of forming HNO3 upon oxidising NO; NO vd (mm/s) = the deposition velocity for remediating NO; nm = not measured; np = not possible to measure using the chosen method; un = unrealistic values obtained and therefore omitted.

refractive materials of nanoscale thickness [36]. The wavelength and spacing between these oscillations was used to determine the coating thickness [49,50]. It should be noted however that some samples produced herein were too hazy, and did not show any oscillations in their UV–visible transmission patterns for their coating thickness to be determined by this method. Coming back to the example shown in Fig. S10a, the sample produced at 450 °C showed a greater number of oscillations than any other in this series, with this corresponding to the growth of a thicker coating (~1058 ± 14 nm). The thickness of all coatings in this series, where determined, are summarised in Table 1. Using the UV–visible transmission data, the indirect optical bandgap (E_{bg}) was determined in all samples using a Tauc plot [34]. An example Tauc plot for sample TTIP-Ox-None-450 is shown in Fig. S10b, where the E_{bg} of ~3.37 eV was obtained. This was close to the expected E_{bg} for a phase pure anatase TiO_2 coating (~3.2 eV) [51]. Expectedly, the sample that contained some rutile TiO_2 (TTIP-Ox-MeOH-550) possessed the lowest E_{bg} (~2.92 eV), as rutile has a more narrow bandgap energy (~3.0 eV) [51]. A bar chart of the E_{bg} of all coatings are plot in Fig. S10c and summarised in Table 1. No trend was observed apart from the tendency for coatings made with no co-oxidant to show E_{bg} closer to the expected literature value for anatase TiO_2. This may be related to differences in the Urbach tail, which is an additional absorption band in the vicinity of the band edge of TiO_2 when defects, bulk or surfaced modifications are present [52]. The average visible light transmittance (VLT) was also determined for all coatings in this series, and are plot in Fig. S10d and summarised in Table 1. Again, there was no obvious trend apart from the fact that the sample that contained rutile (TTIP-Ox-MeOH-550) showed the lowest VLT, which resulted in a rougher film being formed.

3.1.4. *Photocatalytic NO_x activity*

The photocatalytic activity towards NO gas of all samples in the co-oxidant series was measured. Bar charts of the photocatalytic NO and overall NO_x removal, grouped by deposition temperature and then co-oxidant, are shown in Fig. 3. Bar charts of the photocatalytic NO and overall NO_x removal, grouped by co-oxidant used and then deposition temperature are plot in Fig. S11, alongside the selectivity for forming HNO_3 and the deposition velocity of NO removal. Across the board,

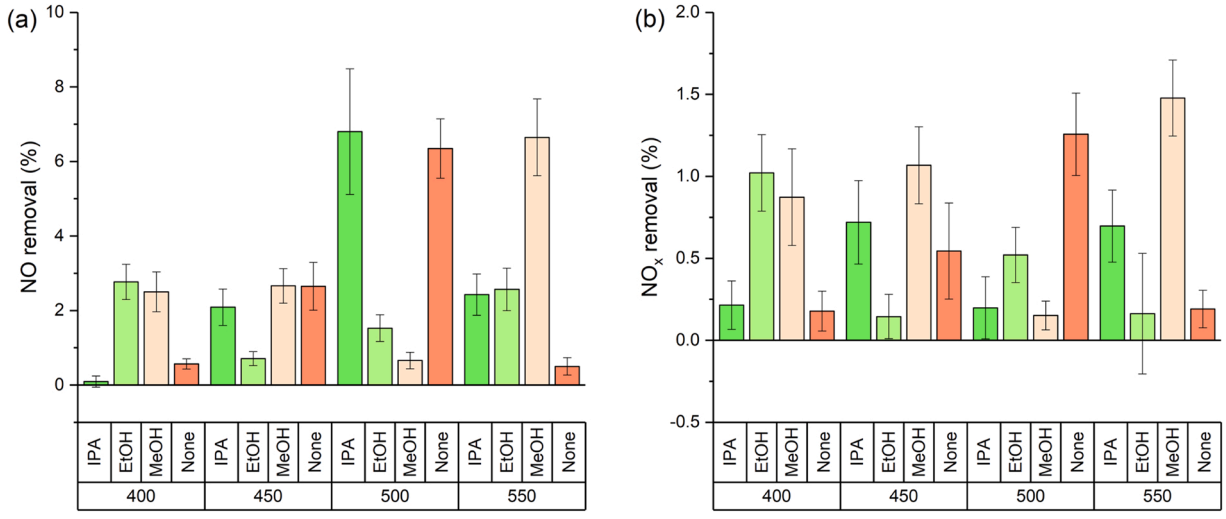

Fig. 3. Bar charts of (a) Photocatalytic NO reduction (%) and (b) NO_x reduction (%), for all TiO_2 coatings in the co-oxidant series, grouped by deposition temperature (400, 450, 500 and 550 °C) and then by co-oxidant used (IPA = isopropanol; EtOH = ethanol; MeOH = methanol; None = no co-oxidant used).

higher photocatalytic NO removal was observed compared with overall NO_x removal. This was attributed to the low selectivity of HNO_3 formation Fig. S11c (up to ~35 %), which meant that the majority of NO was being oxidised to NO_2 (~65 % or more) and not fully to HNO_3. It should be noted that the goal of any commercially applied photocatalytic system for treating NO_x should be to avoid being a net producer of NO_2, as this can worsen air quality instead of improving it [53]. In general, samples that showed high photocatalytic NO removal also showed high overall photocatalytic NO_x removal. However, there were some notable exceptions, with sample TTIP-Ox-IPA-500, for example, showing the highest photocatalytic NO removal but one of the lowest overall NO_x removal. This was because of the low selectivity of converting NO to HNO_3 by this sample (~3 %). The most active sample for overall NO_x removal in this series was TTIP-Ox-MeOH-550, which was the only sample in this series that contained rutile (~34 %) and was the roughest coating in this series too (~144 nm). All photocatalytic activity data for this series is summarised in Table 1

Similar to the above section, the effects of surfactant and precursor solvent are presented in the Supporting Information. In the following sections, we will proceed to analyse all 50 samples produced herein as a collective.

3.2. Transient absorption spectroscopy

The transient absorption decay kinetics of all samples were measured at the probe wavelength of 650 nm using 355 nm laser excitation from the microsecond to second timescale. According to previous studies, the transient absorption at 650 nm in anatase and rutile TiO_2 represents a near equal mixed signature of electron and hole carriers [54,55]. An example transient absorption decay is shown in Fig. S34 for sample Ti $(OBu)_4$-Sol-Toluene-450. Typical power law decay dynamics is seen in this phase pure anatase TiO_2 coating, which is a result of the thermal trapping/de-trapping mediated pathway by which electron-hole recombination occurs [56].

It is well accepted that NO_x oxidation is mediated by hydroxyl ($OH^{\bullet}$) and superoxide ($O_2^{\bullet-}$) radicals that form on the surface of TiO_2, which are generated through reactions of photogenerated holes with water and photogenerated electrons with oxygen, respectively [9]. Previous transient absorption studies have shown that the formation of these radical occur on the microsecond timescale [51]. As such, two key parameters were extracted from each decay: (i) the initial transient absorption seen at 10 μs (mΔO.D. @ 10 μs), which represents the population of charge carriers present at this time and (ii) the time taken for these charges to recombine to half their initial population ($t_{50\%}$). In sample $Ti(OBu)_4$--Sol-Toluene-450, a mΔO.D. @ 10 μs of ~0.20 and $t_{50\%}$ of ~0.28 ms were observed; values which are quite typical of an anatase TiO_2 coating grown by CVD [54].

All samples showed a positive transient absorption signal at 650 nm, with the exception of samples TTIP-Ox-MeOH-550 and $Ti(OBu)_4$-Surf-SDS-0.75 g, which showed bleach signals that may have been caused by a higher concentration of defects or impurities in these materials [57]. Neglecting these two samples, a wide range of mΔO.D. @ 10 μs (from ~0.0 to ~0.30) and $t_{50\%}$ (<0.01 to ~0.60 ms) were seen across the 48 remaining samples (Table S7).

The relationships between synthesis parameters and the observed transient absorption decay behaviours, as well as the relationship between transient absorption decay and photocatalytic NO_x activity, are investigated in the following section.

3.3. Comparisons of all data from the three different growth strategies

3.3.1. The influence of the synthesis parameters on physicochemical properties and photocatalytic NOx activity

Across the 50 samples produced herein, the photocatalytic and physicochemical property data was grouped for various synthetic parameters. These included the precursor used the precursor used (TTIP or $Ti(OBu)_4$), the solvent used (MeOH, EtOH, Toluene, IPA), the deposition temperature (400, 450, 500, 550 °C) and if a surfactant was used (yes, no). Within each group, the data was averaged and the 90 % confidence interval was determined from the standard error.

3.3.1.1. Crystal properties. There was a clear impact on the anatase content for a number of synthesis conditions. When the precursor Ti $(OBu)_4$ was used (N = 25; 92.6 ± 4.2 %), the anatase content was lower than when TTIP was used (N = 25; 98.6 ± 2.2 %) (Fig. 4a). Also, when the solvent MeOH was used, on average, there was a significantly lower anatase content (85.2 %) than when another solvent was used (>98.3 %). And when the higher deposition temperature of 550 °C was used, on average, there was a significantly lower anatase content (88.4 %) than when lower deposition temperatures were used (>98.5 %). However, when examining other crystal properties, there were no significant differences (with 90 % confidence) between any of the synthesis conditions specified above as well as the average anatase crystallite size, anatase unit cell volume or texturing in the anatase (101), (200) or (211) crystal planes (with the exception of there being a greater preference to grow in the (200) plane at 500 °C compared with 450 °C and there being a greater preference to grow in the (211) plane at 450 °C compared with 500 or 550 °C).

3.3.1.2. Surface roughness. The synthetic parameters also had a significant impact on surface roughness (Rq). The use of the precursor Ti $(OBu)_4$ (N = 25; 89.2 ± 32.8 nm) resulted in rougher films than those made using TTIP (N = 25; 29.3 ± 17.4 nm) (Fig. 4b). The use of the solvent MeOH and higher deposition temperatures also resulted in rougher films, which may be attributed to the increased tendency to form anatase: rutile composites, as well as the increased tendency for gas phase precursor decomposition and cluster formation at higher deposition temperatures [58].

3.3.1.3. Optical properties. Likely influenced by anatase content and surface roughness, there were clear relationships between the synthetic parameters used and the indirect bandgap (E_{bg}) and average visible light transmission (VLT), respectively (Fig. 4c). As such, when the solvent MeOH was used, and at higher deposition temperatures, a lower E_{bg} was observed. Similarly, lower VLT was observed, on average, when MeOH (55.7 %) was used compared with any other solvent (> 65.6 %), and at higher deposition temperatures. Also, where the precursor $Ti(OBu)_4$ (N = 25; 61.5 ± 4.0 %) was used, a lower VLT was seen than where TTIP was used (N = 25; 68.1 ± 2.0 %).

3.3.1.4. Photocatalytic NO_x activity. With regards to photocatalytic NO removal, on average, near double the NO removal was seen when the precursor $Ti(OBu)_4$ (N = 25; 4.63 ± 1.17 %) was used to produce the coating compared with TTIP (N = 25; 2.32 ± 0.62 %) (Fig. 4d). No significant differences were seen for the solvents MeOH (N = 13; 3.55 ± 1.07 %), EtOH (N = 13; 3.36 ± 1.40 %) and Toluene (N = 20; 3.84 ± 1.35 %); however, the use of IPA (N = 4; 1.77 ± 0.74 %) resulted in significantly less active films. Photocatalytic NO removal increased with deposition temperature, from 2.34 ± 0.84 % at 400 °C (N = 8) to 4.79 ± 2.25 % at 500 °C (N = 8), and then decreased marginally to 3.77 ± 1.15 % at 550 °C (N = 17). And the use of a surfactant resulted in a near halving of photocatalytic NO removal activity, on average, from 4.08 ± 0.94 % (N = 34) to 2.20 ± 0.74 % (N = 16). Overall, this analysis indicates that TiO_2 coatings produced using the precursor $Ti(OBu)_4$, in either MeOH, EtOH or Toluene at 500 °C with no surfactant would produce the most active films for photocatalytic NO removal, where this group contained the 2nd and 3rd most active materials produced herein ($Ti(OBu)_4$-Sol-EtOH-500 and $Ti(OBu)_4$-Sol-Toluene-500, respectively). With regards to photocatalytic NO_x removal, near analogous trends to photocatalytic NO removal were observed (Fig. S35a). However, larger relative confidence intervals were present, and all that could be said

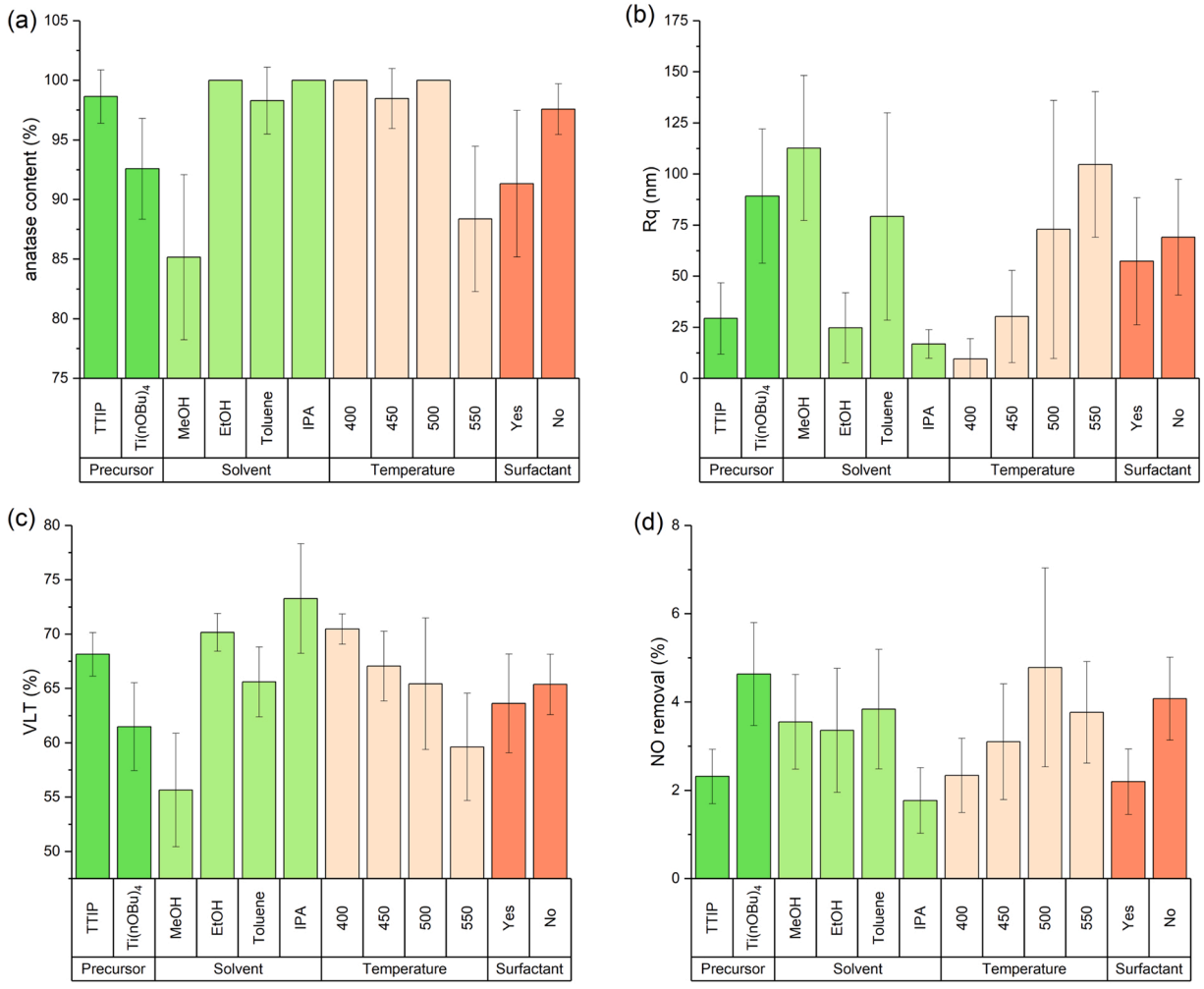

Fig. 4. Bar chart plots of the average and standard error (90 % confidence intervals) for (a) anatase content (%), (b) root mean squared (Rq) surface roughness (nm), (c) average visible light transmittance (380–750 nm) and (d) photocatalytic NO removal (%) for all TiO_2 coatings produced herein grouped by various specified synthetic condition; precursor used (TTIP or $Ti(OBu)_4$), solvent used (MeOH, EtOH, Toluene, IPA), Temperature (400, 450, 500, 550 °C) or surfactant used (yes, no).

with 90 % confidence was that coatings made using $Ti(OBu)_4$ (N = 25; 1.14 ± 0.38 %) were far more active for photocatalytic NO_x removal compared with coatings made using TTIP (N = 25; 0.44 ± 0.14 %), and that the use of surfactant was detrimental to photocatalytic NO_x removal. On the other hand, with regards to the selectivity of forming HNO_3 upon oxidising NO, quite different trends were observed, where the choice of precursor and surfactant had no significant impact (Fig. S35b). Contrastingly, the selectivity of forming HNO_3 was significantly higher when the solvent IPA was used and for samples made at 400 °C.

3.3.1.5. Transient absorption decay kinetics. Comparing charge carrier populations measured at 10 μs, the use of precursor had no significant influence on these populations (Fig. S35c). However, the use of the precursor solvent Toluene (N = 20; 0.11 ± 0.03 mΔO.D.) resulted in coatings with significantly higher charge carrier populations than MeOH (N = 13; 0.04 ± 0.01 mΔO.D.) and IPA (N = 4; 0.04 ± 0.03 mΔO.D.). With regards to charge carrier lifetime from 10 μs ($t_{50\%}$), the use of the precursor solvent MeOH and higher deposition temperatures tended to produce coatings with higher charge carrier lifetimes than other solvents (Fig. S35d). This may be due to the greater tendency to form some rutile TiO_2 when both MeOH and higher deposition temperatures were are used, resulting in enhanced lifetime due to charge transfer between anatase and rutile sites [55].

3.3.2. The influence of physicochemical properties on photocatalytic NO_x activity

3.3.2.1. Crystal properties. Using scatter plots, the relationship between the crystal properties and photocatalytic NO and NO_x removal were assessed using data from all coatings produced herein (50 samples). Scatter plots of anatase content versus photocatalytic NO (r^2 ~0.01) and NO_x (r^2 ~0.00) removal indicated that there was no correlation between crystal phase and photocatalytic NO_x activity for the coatings produced herein (Fig. S36). Similarly, scatter plots of anatase crystallite size versus photocatalytic NO (r^2 ~0.01) and NO_x (r^2 ~0.01) removal (Fig. S37), and scatter plots of anatase unit cell volume versus photocatalytic NO (r^2 ~0.04) and NO_x (r^2 ~0.04) removal (Fig. S38) indicated that there was no correlation for these crystal properties too. However, plots of the texture coefficients for the (101), (200) and (211) anatase crystal planes (Fig. S39) showed that there were weak correlations between the (200) (r^2 ~0.14) and (211) (r^2 ~0.14) crystal planes and photocatalytic NO removal, and no correlation between the (101) (r^2 ~0.00) crystal plane and photocatalytic NO removal.

3.3.2.2. Surface roughness. Scatter plots of surface roughness (Rq) versus photocatalytic NO removal (r^2 ~0.21) (Fig. S40a) and surface roughness factor (Rf) versus photocatalytic NO removal (r^2 ~0.11) (Fig. S41b) revealed weak correlations. However, next to no correlation was seen in scatter plots of surface roughness (Rq) versus photocatalytic

NO_x removal (r^2 ~0.05) (Fig. S40b) and surface roughness factor (Rf) versus photocatalytic NO_x removal (r^2 ~0.04) (Fig. S41b).

3.3.2.3. Optical properties. No relationship between film thickness and photocatalytic NO (r^2 ~0.00) and NO_x (r^2 ~0.02) removal was observed herein (Fig. S42). This was expected, as film thicknesses herein were greater than the expected hole diffusion length for anatase and rutile TiO_2 [59]. No correlation was also seen between the bandgap energy (E_{bg}) and photocatalytic NO (r^2 ~0.07) and NO_x (r^2 ~0.00) removal. However, a weak relationship was observed between the average visible light transmittance (VLT) and photocatalytic NO removal, where higher activity was observed at lower VLT (r^2 ~0.11) (Fig. 5a). Incidentally, what this figure shows is that when films are more rough and scattering, in general, their photocatalytic activity towards NO removal increases. This is likely due to an increase in catalytic surface area, which is supported by the correlations observed between surface roughness (Rq) and photocatalytic NO removal (r^2 ~0.21) (Fig. S40a).

3.3.2.4. Transient absorption decay kinetics. With respect to the charge carrier dynamics measured herein, a weak correlation was observed between photocatalytic NO removal and the charge carrier population measured at 10 μs (r^2 ~0.11) (Fig. S43a), and no correlation was observed between photocatalytic NO removal and the charge carrier lifetime ($t_{50\%}$ from 10 μs) (r^2 ~0.00) (Fig. S43b). This relationship was similar for photocatalytic NO_x removal, with the charge carrier population measured at 10 μs (r^2 ~0.11) showing a marginally stronger correlation than the charge carrier lifetime (r^2 ~0.02).

3.3.2.5. A linear combination model for estimating the contribution of each physicochemical property on the photocatalytic activity. In the previous sections, scatter plots of various physicochemical properties, obtained from the physical characterisation of the 50 coatings produced herein, were plot against their measured photocatalytic NO and NO_x removal activities. Although some weak correlations were observed - with the strongest correlation being between surface roughness (Rq) and photocatalytic NO removal (r^2 ~0.21) (Fig. S40a) - it was clear that no one physicochemical property could be used to fully explain the photocatalytic NO and NO_x removal activities observed herein. This is attributed to the complexity of any photochemical reaction, which is controlled by a number of factors, which include the population of charge carriers formed, their lifetime, their ability to diffuse to the surface of the photocatalyst, their energy and reaction kinetics, and the concentrations of the reaction species involved; all of which are controlled by the various intrinsic physicochemical properties of the

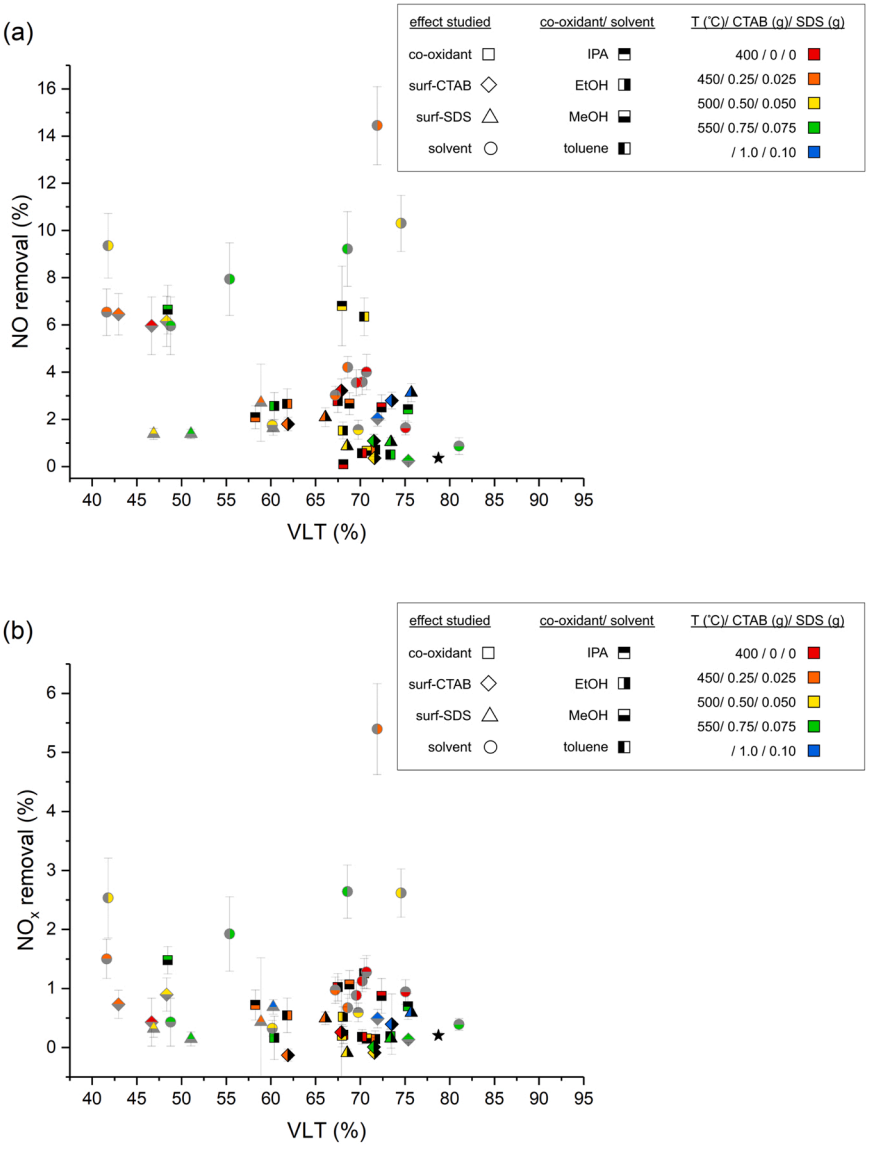

Fig. 5. Scatter plots of the average visible light transmittance (VLT (%); 380–750 nm) against photocatalytic (a) NO reduction (%) and (b) NO_x reduction (%) for all TiO_2 coatings produced herein. The data is categorised by the effect studied (symbol shape), co-oxidant/ solvent used (symbol interior section filled), deposition temperature (°C)/ surfactant added (g) (symbol fill colour) and precursor used (black outline = TTIP; grey outline = Ti $(OBu)_4$). (For interpretation of the references to colour in this figure legend, the reader is referred to the web version of this article.)

material [60,61]. To rationalise the influence of each physicochemical property characterised herein on the photocatalytic NO and NO_x removal activity, we devised a simple model. The physicochemical properties included in this model were: (i) anatase content, (ii) average crystal size, (iii) unit cell volume, (iv) to (vi) texture coefficients for anatase (101), (200) and (211) planes, (vii) E_{bg}, (viii) VLT, (ix) Rq, (x) charge carrier population at 10 μs and (xi) charge carrier lifetime from 10 μs. In this model, the data for each of these 11 physicochemical parameters and photocatalytic NO and NO_x removal activity was scaled to be between 0 and 1. Each of these 11 physicochemical parameters were multiplied by a factor that was set to be between −1 and 1. The sum of these factors, multiplied by their corresponding physicochemical parameter, was termed the *predicted photocatalytic activity* (PPA):

$$PPA_i = \sum(ax_a + bx_b + \ldots kx_k) \tag{6a}$$

where x_a to x_k represent the 11 normalised physicochemical properties measured for the i^{th} sample and a to k represent factors used to multiply each physicochemical property for the i^{th} sample. The sum of the absolute values of the 11 factors was constricted to total 1:

$$\sum(|a| + |b| + \ldots |k|) = 1 \tag{6b}$$

Therefore, these factors essentially gauged the degree of positive or negative influence each physicochemical parameter had on the PPA. The PPA was compared with the *observed photocatalytic activity* (OPA) for each sample, and the factors were systematically varied to achieved the lowest possible error:

$$X^2 = \sum\left|\frac{(OPA - PPA)^2}{PPA}\right| \tag{6c}$$

It should be noted that the surface roughness was not measured for all samples, and therefore, data from only 27 samples (of the 50 produced herein) was included in the model.

For photocatalytic NO removal, the lowest X^2 that could be achieved between OPA and PPA was 2.17 (Table S8). A scatter plot of OPA against PPA revealed a moderate positive correlation (r^2 ~0.74) (Fig. S44a), with a Pearson's correlation coefficient of 0.90. Looking at the factors that make up the PPA, several physicochemical parameters had near zero factors - anatase content, average crystal size, unit cell volume, E_{bg} and VLT - and therefore did not likely contribute to the OPA. The preferred growth in the (101) and (200) anatase planes were indicated by the model to have positive influences on the OPA (~5 and ~7 %, respectively), whereas preferred growth in the (211) anatase plane was indicated by the model to have a negative influence on the OPA (−11 %). The physicochemical parameters that had the largest influence on the OPA were Rq (24 %), charge carrier population at 10 μs (21 %) and charge carrier lifetime from 10 μs (31 %). This was despite there being a near zero correlation seen between charge carrier lifetime and photocatalytic NO activity on a scatter plot (Fig. S43b), and therefore reinforced the idea that photocatalysis is governed by a number of physicochemical properties.

For photocatalytic NO_x removal, the lowest X^2 that could be achieved between OPA and PPA was 1.89 (Table S8). A scatter plot of OPA against PPA revealed a positive correlation (r^2 ~0.69) (Fig. S44b), with a Pearson's correlation coefficient of 0.85. Interestingly, there were some notable changes in the factors that make up the PPA compared with the model for photocatalytic NO removal. For example, preferred growth in the (101) and (200) anatase planes now had near zero influence on the observed activity. Also, the average crystal size showed a small negative influence on activity (~−5 %). And interestingly, the E_{bg} had a moderate influence on activity (~15 %), which may be related to the energetics of the conduction and valence bands that drive the oxidation of NO to HNO_3. However, consistent with the model for photocatalytic NO removal, the largest influencers on the observed activity for NO_x removal were Rq (16 %), charge carrier population at 10 μs (27 %) and charge carrier lifetime from 10 μs (19 %).

Although both models showed good general agreement between the PPA and OPA, there were some individual cases where the PPA differed quite substantially from the OPA. For example, in the photocatalytic NO model, the PPA (0.54) of most active sample $Ti(OBu)_4$-Sol-Toluene-450 deviated largely from the OPA (1.0). This indicated that the suite of physicochemical properties measured herein, and incorporated in our model, were not sufficient to account for all OPA. For example, it is known that a photocatalytic reaction is controlled by the ability of charge carriers to diffuse from where they are formed to the surface of the material where reactions occur; [61] however, none of the physical characterisation methods applied herein can measure the mobility of photogenerated charges. Similarly, it is also known that a photocatalytic reaction is controlled by the energy of the charge carriers formed, which is often controlled by the band energetics. Again, none of the physical characterisation methods applied herein can measure the energy of charge carriers or band energetics. As such, for a more rigorous, and likely, more precise model, further physical characterisation of our coatings would be required (e.g. the use of terahertz spectroscopy to determine charge carrier mobility [62] and the use of Kelvin probe force spectroscopy to measure band energetics [63], etc.). Another reason for the differences seen between the PPA and OPA in our model may have been caused by the error in our assumption that the physical properties measured at the centre of the coating (~1 cm^2 area) are a sound proxy for the physical properties seen across the entire coating (~50 cm^2), which was used in the photocatalytic test. And lastly, the model used herein is simplistic, and can only be used to estimate the contribution of each physicochemical property to the OPA. The use of more formally accepted models for PPA may improve the accuracy of the prediction [64].

3.3.3. Comparisons with the literature

To our knowledge, the photocatalytic NO_x activity of TiO_2 thin films on glass have rarely been examined, and could only find one instance [16]. Langridge et al. examined the commercial self-cleaning glass, Pilkington Activ™, which employs an ultra-thin (~12 nm) and smooth (Rq ~2.3 nm) coating of TiO_2 [65]. This was tested using conditions that differed substantially from ISO protocol, and used NO_2 as the test gas as opposed to NO. They found that their baseline concentration of NO_2 dropped from ~0.07 ppm to ~0.04 ppm under the action of photocatalysis [16]. For fair comparison, the photocatalytic NO_x activity of Pilkington Activ™ was measured using the same protocol as the 50 samples produced and tested herein. It should be noted that Pilkington Activ™ is produced using a traditional CVD route, whereas the 50 samples examined herein were produced using an aerosol-assisted route. Pilkington Activ™ showed a NO removal of 0.36 ± 0.16 % and NO_x removal of 0.20 ± 0.05 %. Comparing this against our most active sample, $Ti(OBu)_4$-Sol-Toluene-450, the NO and NO_x removal activities were ~40 and ~25 times lower, respectively. However, it should be noted that this comparatively lower photocatalytic activity is understandable, since according to Zouzelka et al., Pilkington Activ™ was designed with the purpose of achieving only a nominal self-cleaning efficacy whilst retaining the strict, high VLT required for glazing applications [66]. Herein, Pilkington Activ™ showed a VLT of ~80 %, and our best performing sample showed a VLT of ~72 %. Typical 'clear glass' applications require a VLT of 80 % and above. We suspect that reducing the film thickness of our best performing sample can result in a VLT of 80 % being reached. Nevertheless, there are applications of glass that do not require high transparency, such as in cladding and privacy windows, where samples that show high photocatalytic NO_x activity and low VLT may be applicable.

Our best performing sample was examined under ISO conditions for the full 5 hr irradiation period (Fig. S45). Over the entire test, the sample showed reductions in NO and NO_2 of ~8.2 ± 0.70 % and ~0.80 ± 0.14 %, respectively. This was significantly lower than what was observed in the 1 hr long test (carried out for the 50 samples produced herein),

where reductions in NO and NO_2 of ~14.4 ± 1.7 % and ~5.4 ± 0.77 %, respectively, were observed (Table S6). However, if we break down the performance measured under ISO conditions by the first and last hr of the test, then we see reductions in NO and NO_2 of ~14.9 ± 1.8 % and ~2.4 ± 0.47 %, respectively, for the first hr and reductions in NO and NO_2 of ~5.9 ± 0.49 % and ~0.09 ± 0.04 %, respectively, for the last hr. The performance seen in the first hr of the ISO test was quite similar to performance seen in the 1 hr long test. However, the performance seen in the last hr of the ISO test was significantly reduced, with little to no reduction in NO_x shown by the material, with the material essentially becoming an NO to NO_2 converter [67]. This test showed that this material, over prolonged testing, losses its ability to remediate NO_x; most likely due to the surface of the photocatalyst becoming saturated with HNO_3, and therefore, requiring washing to restore its function [13].

In the field of developing TiO_2-based coatings on building materials for NO_x remediation, more porous and high surface area materials are more often studied than glass [15]. Building materials such as concrete (~7–45 %), paint (~14 – 70 %) and asphalt (~42 – 67 %) often show significantly higher photocatalytic NO removal activity compared with the glass studied herein (~0.1–14.4 %). Russell et al. found that the substrate material has a significant effect on the observed photocatalytic activity, concluding that substrates with rougher surfaces tend to show higher activity. [68] Also, considering the relatively higher toxicity of NO_2 compared with NO, driving the oxidation of NO to HNO_3 with high selectivity is desirable. Across the 50 TiO_2 samples produced herein, the average selectivity of HNO_3 formation was ~25 %, which is similar to commercial TiO_2 products such as Aeroxide P25 (~28 %) and Hombikat UV100 (~27 %) [53]. However, recent studies have shown that doping the photocatalyst or the addition of surface catalysts to the photocatalyst can increase the selectivity of HNO_3 formation to near unity [53,69]. Moreover, van de Krol et al. have shown that it may be possible to avoid the possible toxicity issues that surround oxidising NO by selectively reducing it to N_2 using oxygen vacancy-rich TiO_2 [70].

4. Conclusions

Herein, we applied AA-CVD to produce TiO_2 coatings on window glass and examine their photocatalytic activity towards NO gas. A range of process parameters were explored to produce 50 unique TiO_2 coatings possessing wide ranging physicochemical properties. For these 50 unique samples, the links between process parameters, physicochemical properties and photocatalytic activity towards NO gas were studied. Our results showed which process parameters had the strongest influence on the observed activity, with TiO_2 coatings produced using the precursor $Ti(OBu)_4$, in either MeOH, EtOH or Toluene at 500 °C with no surfactant showing the highest photocatalytic activity. Our results also showed that the three most influential physicochemical properties on the observed photocatalytic activity were surface roughness (Rq), charge carrier population (at 10 μs) and charge carrier lifetime (from 10 μs). Supporting this outcome, samples produced using Toluene or MeOH showed the highest charge carrier populations and lifetimes, respectively, and produced some of the roughest coatings.

Importantly, this study identified a number of AA-CVD routes to TiO_2 coatings on window glass that showed significantly higher photocatalytic activity towards NO gas than a commercially available self-cleaning window, Pilkington NSG Activ™, and therefore, can be used as a guide for future work on the development of photocatalytic coatings for applications in NO_x remediation.

CRediT authorship contribution statement

Yanda Wong did the majority of synthesis and testing herein. **Zhipeng Lin** carried out ISO testing of the best performing sample. **Yuankai Li** did AFM measurements. **Andreas Kafizas** curated and analysed the data, and wrote the publication.

Declaration of Competing Interest

The authors declare that they have no known competing financial interests or personal relationships that could have appeared to influence the work reported in this paper.

Data availability

Data will be made available on request.

Acknowledgements

A. K. thanks the EPSRC for a Capital Award Emphasising Support for Early Career Researchers and the Royal Society for an Equipment Grant (RSG\R1\180434). Y. W. thanks Dr. Ecaterina Ware for support with SEM imaging. Lee Tooley and Steve Atkins are thanked for constructing the chemical vapour deposition apparatus used herein. Pilkington NSG are thanked for providing the Pilkington Optifloat™ float glass and Pilkington Activ™ self-cleaning glass used in this work.

Appendix A. Supporting information

Supplementary data associated with this article can be found in the online version at doi:10.1016/j.apcata.2022.118924.

References

[1] Nitrogen Dioxide in the United Kingdom - UK Air Quality Expert Group. (2004).
[2] O. Carp, C.L. Huisman, A. Reller, Photoinduced reactivity of titanium dioxide, Prog. Solid State Chem. 32 (2004) 33–177.
[3] UK Plan for Tackling Roadside Nitrogen Dioxide Concentrations: an Overview. (2017).
[4] Coules, C. Hidden harms: the impacts of air pollution on the mind, AirQualityNews (2021).
[5] Carrington, D. Air pollution linked to more severe mental illness – study,The Guardian (2021).
[6] R. Delmas, D. Serça, C. Jambert, Global inventory of NOx sources, Nutr. Cycl. Agroecosyst. 48 (1997) 51–60.
[7] GOV.UK. Emissions of air pollutants in the UK – Nitrogen oxides (NOx). (2022). Available at: https://www.gov.uk/government/statistics/emissions-of-air-pollutants/emissions-of-air-pollutants-in-the-uk-nitrogen-oxides-nox#major-emission-sources-for-nitrogen-oxides-in-the-uk. (Accessed: 12th August 2022)
[8] Y. Boyjoo, H. Sun, J. Liu, V.K. Pareek, S. Wang, A review on photocatalysis for air treatment: From catalyst development to reactor design, Chem. Eng. J. 310 (2017) 537–559.
[9] J. Balbuena, M. Cruz-Yusta, L. Sánchez, Nanomaterials to combat NOX pollution, J. Nanosci. Nanotechnol. 15 (2015) 6373–6385.
[10] J. Lasek, Y.H. Yu, J.C.S. Wu, Removal of NOx by photocatalytic processes, J. Photochem. Photobiol. C Photochem. Rev. 14 (2013) 29–52.
[11] J. Ângelo, L. Andrade, L.M. Madeira, A. Mendes, An overview of photocatalysis phenomena applied to NOx abatement, J. Environ. Manag. 129 (2013) 522–539.
[12] J. Schneider, et al., Understanding TiO2 Photocatalysis: Mechanisms and Materials, Chem. Rev. 114 (2014) 9919–9986.
[13] N. Serpone, Heterogeneous photocatalysis and prospects of TiO2-based photocatalytic DeNOxing the atmospheric environment, Catalysts 8 (2018).
[14] A. Mills, R. Andrews, R. Han, C. O'Rourke, S. Hodgen, Supersensitive test of photocatalytic activity based on ISO 22197-1:2016 for the removal of NO, J. Photochem. Photobiol. A Chem. 400 (2020), 112734.
[15] EIC. Towards purer air: a Review of the Latest Evidence of the Effectiveness of Photocatalytic Materials and Treatments in Tackling Local Air Pollution (2018).
[16] J.M. Langridge, et al., Solar driven nitrous acid formation on building material surfaces containing titanium dioxide: A concern for air quality in urban areas? Atmos. Environ. 43 (2009) 5128–5131.
[17] A. Mills, et al., Characterisation of the photocatalyst Pilkington Activ (TM): a reference film photocatalyst? J. Photochem. Photobiol. A Chem. 160 (2003) 213.
[18] Kafizas, A. , Parkin, I.P. Materials for a Sustainable Future, Chapter 20 - Glass and New Technologies, The Royal Society of Chemistry, 2012.
[19] K. Choy, Chemical vapour deposition of coatings, Prog. Mater. Sci. 48 (2003) 57–170.
[20] P. Marchand, I.A. Hassan, I.P. Parkin, C.J. Carmalt, Aerosol-assisted delivery of precursors for chemical vapour deposition: expanding the scope of CVD for materials fabrication, Dalton Trans. 42 (2013) 9406–9422.
[21] C.S. Mc Nally, D.P. Turner, A.N. Kulak, F.C. Meldrum, G. Hyett, The use of cationic surfactants to control the structure of zinc oxide films prepared by chemical vapour deposition, Chem. Commun. 48 (2012) 1490–1492.
[22] X. Hou, K.L. Choy, Processing and applications of aerosol-assisted chemical vapor deposition, Chem. Vap. Depos. 12 (2006) 583–596.

[23] Physical Sciences Data science Service. https://www.psds.ac.uk/. (Accessed 27th September 2019).
[24] B.H. Toby, EXPGUI a graphical user interface for GSAS, J. Appl. Crystallogr. 34 (2001) 210–213.
[25] A. Kafizas, et al., Where do photogenerated holes Go in anatase:rutile TiO2? A transient absorption spectroscopy study of charge transfer and lifetime, J. Phys. Chem. A 120 (2016) 715–723.
[26] A.L. Patterson, The Scherrer formula for X-ray particle size determination, Phys. Rev. 56 (1939) 978–982.
[27] A.C.L. Dreele, R.B. Von, Gen. Struct. Anal. Syst. (GSAS) 748 (2004).
[28] B.V. Diesen, M. Jonsson, I.P. Parkin, Improved texturing and photocatalytic efficiency in TiO2 films grown using aerosol-assisted CVD and atmospheric pressure CVD, Chem. Vap. Depos. 19 (2013) 355–362.
[29] E.P. Meagher, G.A. Lager, Polyhedral thermal expansion in the TiO2 polymorphs; refinement of the crystal structures of rutile and brookite at high temperature, Can. Mineral. 17 (17) (1979) 77–85.
[30] R. Restori, D. Schwarzenbach, J.R. Schneider, Charge density in rutile, TiO2, Acta Crystallogr. Sect. B 43 (1987) 251–257.
[31] M. Horn, C.F. Schwebdtfeger, E.P. Meagher, Refinement of the structure of anatase at several temperatures, Cryst. Mater. 136 (1972) 273–281.
[32] P. D Antonio, M. Lasalvia, G. Perna, V. Capozzi, Scale-independent roughness value of cell membranes studied by means of AFM technique, Biochim. Biophys. Acta Biomembr. 1818 (2012) 3141–3148.
[33] P.J. Ramón-Torregrosa, M.A. Rodríguez-Valverde, A. Amirfazli, M.A. Cabrerizo-Vílchez, Factors affecting the measurement of roughness factor of surfaces and its implications for wetting studies, Colloids Surf. A Physicochem. Eng. Asp. 323 (2008) 83–93.
[34] J. Tauc, Optical properties and electronic structure of amorphous Ge and Si, Mater. Res. Bull. 3 (1968) 37–46.
[35] L. Yin, et al., Semitransparent polymer solar cells floating on water: selected transmission windows and active control of algal growth, J. Mater. Chem. C 9 (2021) 13132–13143.
[36] R.J. Swanepoel, Determination of the thickness and optical constants of amorphous silicon, J. Phys. E 16 (1983) 1214–1222.
[37] J.R. DeVore, Refractive indices of rutile and sphalerite, J. Opt. Soc. Am. 41 (1951) 416–419.
[38] J. Patzsch, A. Folli, D.E. Macphee, J.Z. Bloh, On the underlying mechanisms of the low observed nitrate selectivity in photocatalytic NOx Abatement and the importance of the oxygen reduction reaction, Phys. Chem. Chem. Phys. 19 (2017) 32678–32686.
[39] A. Kafizas, C.R. Crick, I.P. Parkin, The combinatorial atmospheric pressure chemical vapour deposition (cAPCVD) of a gradating substitutional/interstitial N-doped anatase TiO2 thin-film; UVA and visible light photocatalytic activities, J. Photochem. Photobiol. A Chem. 216 (2010) 156–166.
[40] G. Hyett, M. Green, I.P. Parkin, X-ray diffraction area mapping of preferred orientation and phase change in TiO2 thin films deposited by chemical vapor deposition, J. Am. Chem. Soc. 128 (2006) 12147–12155.
[41] C. Sotelo-Vazquez, et al., Multifunctional P-doped TiO2 films: a new approach to self-cleaning, transparent conducting oxide materials, Chem. Mater. 27 (2015) 3234.
[42] A. Jiamprasertboon, et al., Heterojunction α-Fe2O3/ZnO films with enhanced photocatalytic properties grown by aerosol-assisted chemical vapour deposition, Chem. Eur. J. 25 (2019) 11337–11345.
[43] T.E. Weirich, M. Winterer, S. Seifried, H. Hahn, H. Fuess, Rietveld analysis of electron powder diffraction data from nanocrystalline anatase, TiO2, Ultramicroscopy 81 (2000) 263–270.
[44] M. Okrusch, et al., Intergrown niobian rutile phases with Sc- and W-rich ferrocolumbite: an electron-microprobe and Rietveld study, Am. Mineral. 88 (2003) 986–995.
[45] Zhang, Q. Chemical Vapor Deposition to Titanium Dioxide Thin Films. (1993).
[46] Q. Zhang, C. Li, Pure anatase phase titanium dioxide films prepared by mist chemical vapor deposition, Nanomaterials 8 (2018).
[47] C. Edusi, G. Hyett, G. Sankar, I.P. Parkin, Aerosol-assisted CVD of titanium dioxide thin films from methanolic solutions of titanium tetraisopropoxide; Substrate and aerosol-selective deposition of rutile or anatase, Chem. Vap. Depos. 17 (2011) 30–36.
[48] M. Taylor, R.C. Pullar, I.P. Parkin, C. Piccirillo, Nanostructured titanium dioxide coatings prepared by aerosol assisted chemical vapour deposition (AACVD), J. Photochem. Photobiol. A Chem. 400 (2020).
[49] A. Kafizas, C.W. Dunnill, I.P. Parkin, Combinatorial atmospheric pressure chemical vapour deposition (cAPCVD) of niobium doped anatase; effect of niobium on the conductivity and photocatalytic activity, J. Mater. Chem. 20 (2010) 8336–8349.
[50] A. Kafizas, I.P. Parkin, The combinatorial atmospheric pressure chemical vapour deposition (cAPCVD) of a gradating N-doped mixed phase titania thin film, J. Mater. Chem. 20 (2010) 2157–2169.
[51] A. Fujishima, X. Zhang, D. Tryk, TiO2 photocatalysis and related surface phenomena, Surf. Sci. Rep. 63 (2008) 515–582.
[52] P. Makuła, M. Pacia, W. Macyk, How to correctly determine the band gap energy of modified semiconductor photocatalysts based on UV-Vis spectra, J. Phys. Chem. Lett. 9 (2018) 6814–6817.
[53] J.Z. Bloh, A. Folli, D.E. Macphee, Photocatalytic NOx abatement: why the selectivity matters, RSC Adv. 4 (2014) 45726–45734.
[54] X. Wang, et al., Transient absorption spectroscopy of anatase and rutile: the impact of morphology and phase on photocatalytic activity, J. Phys. Chem. C 119 (2015) 10439–10447.
[55] A. Kafizas, et al., Where do photo-generated holes Go in anatase:rutile TiO2? A transient absorption spectroscopy study of charge transfer and lifetime, J. Phys. Chem. A 120 (2016) 715–723.
[56] B. Moss, et al., Comparing photoelectrochemical water oxidation, recombination kinetics and charge trapping in the three polymorphs of TiO2, Sci. Rep. 7 (2017) 2938.
[57] N.P. Chadwick, et al., Ultraviolet radiation induced dopant loss in a TiO2 photocatalyst, ACS Catal. 7 (2017) 1485–1490.
[58] M. Ling, C. Blackman, Growth mechanism of planar or nanorod structured tungsten oxide thin films deposited via aerosol assisted chemical vapour deposition (AACVD), Phys. Status Solidi C 877 (2015) 869–877.
[59] T. Luttrell, et al., Why is anatase a better photocatalyst than rutile? Model studies on epitaxial TiO2 films, Sci. Rep. 4 (2014) 4043.
[60] R. Godin, A. Kafizas, J. Durrant, Electron transfer dynamics in fuel producing photosystems, Curr. Opin. Electrochem. 2 (2017) 136–143.
[61] A. Mills, S. Le Hunte, An overview of semiconductor photocatalysis, J. Photochem. Photobiol. A Chem. 108 (1997) 1–35.
[62] A. Saeki, Y. Yasutani, H. Oga, S. Seki, Frequency-modulated gigahertz complex conductivity of TiO2 nanoparticles: interplay of free and shallowly trapped electrons, J. Phys. Chem. C 118 (2014) 22561–22572.
[63] M.C. Wu, et al., Photo-Kelvin probe force microscopy for photocatalytic performance characterization of single filament of TiO2 nanofiber photocatalysts, J. Mater. Chem. A 1 (2013) 5715–5720.
[64] A. Mills, C. O'Rourke, Revised disrupted langmuir-adsorption model of photocatalysis, J. Phys. Chem. C 119 (2015) 19941–19946.
[65] P. Chin, D.F. Ollis, Decolorization of organic dyes on Pilkington Activ™ photocatalytic glass, Catal. Today 123 (2007) 177.
[66] R. Zouzelka, J. Rathousky, Photocatalytic abatement of NOx pollutants in the air using commercial functional coating with porous morphology, Appl. Catal. B Environ. 217 (2017) 466–476.
[67] A. Mills, S. Elouali, The nitric oxide ISO photocatalytic reactor system: measurement of NOx removal activity and capacity, J. Photochem. Photobiol. A Chem. 305 (2015) 29–36.
[68] H.S. Russell, O. Hertel, T. Ellerman, S.S. Jensen, A review of photocatalytic materials for urban NOx remediation, Catalysts 11 (2021) 1–45.
[69] J.Z. Bloh, R. Dillert, D.W. Bahnemann, Ruthenium-modified zinc oxide, a highly active vis-photocatalyst: the nature and reactivity of photoactive centres, Phys. Chem. Chem. Phys. 16 (2014) 5833–5845.
[70] Q. Wu, R. Van De Krol, Selective photoreduction of nitric oxide to nitrogen by nanostructured TiO2 photocatalysts: role of oxygen vacancies and iron dopant, J. Am. Chem. Soc. 134 (2012) 9369–9375.